Optics Letters

Size-scaling effects for microparticles and cells manipulated by optoelectronic tweezers

Shuailong Zhang,[1,2,3,6] Weizhen Li,[4] Mohamed Elsayed,[1,3] Pengfei Tian,[5] Alasdair W. Clark,[4] Aaron R. Wheeler,[1,2,3] and Steven L. Neale[4,*]

[1]Donnelly Centre for Cellular and Biomolecular Research, University of Toronto, Toronto, Ontario M5S 3E1, Canada
[2]Department of Chemistry, University of Toronto, Toronto, Ontario M5S 3H6, Canada
[3]Institute for Biomaterials and Biomedical Engineering, University of Toronto, Toronto, Ontario M5S 3G9, Canada
[4]School of Engineering, University of Glasgow, Glasgow G12 8LT, UK
[5]Institute for Electric Light Sources, Fudan University, Shanghai 200433, China
[6]e-mail: shuailong.zhang@utoronto.ca
*Corresponding author: Steven.Neale@glasgow.ac.uk

Received 27 June 2019; revised 19 July 2019; accepted 20 July 2019; posted 22 July 2019 (Doc. ID 370856); published 22 August 2019

In this work, we investigated the use of optoelectronic tweezers (OET) to manipulate objects that are larger than those commonly positioned with standard optical tweezers. We studied the forces that could be produced on differently sized polystyrene microbeads and MCF-7 breast cancer cells with light-induced dielectrophoresis (DEP). It was found that the DEP force imposed on the bead/cell did not increase linearly with the volume of the bead/cell, primarily because of the non-uniform distribution of the electric field above the OET bottom plate. Although this size-scaling work focuses on microparticles and cells, we propose that the physical mechanism elucidated in this research will be insightful for other micro-objects, biological samples, and micro-actuators undergoing OET manipulation.

https://doi.org/10.1364/OL.44.004171

Optoelectronic tweezers (OET) is a useful optofluidic technology that relies on light-induced dielectrophoresis (DEP) for many micromanipulation applications [1–4]. To date, OET has been used to control and manipulate many different nano- and micro-scale objects, including nanowires, nanoparticles [2,5], cells, and microparticles [6–9]. More recently, OET was demonstrated to be capable of manipulating large photonic/electronic components [10,11] with sizes greater than 150 micrometers. This suggests an important role of OET as an optical micromanipulation tool to manipulate objects with a wide range of sizes. Therefore, in this work, we studied how the size of the manipulated object affects the forces and manipulation velocities that can be produced with OET, which is important for clarifying the effectiveness of OET as a micromanipulation tool. We propose that the results and methods presented here will be valuable for users looking to optimize OET settings for efficient manipulation of micro-objects over a wide range of scales and experimental conditions.

Figure 1(a) shows a three-dimensional (3D) schematic of the OET device, which comprises two planar electrodes separated by a spacer. The electrodes were formed from a glass slide coated on one side with a 600-nm-thick layer of indium tin oxide (ITO) (Diamond Coatings, UK). The bottom electrode was coated with an additional photoconductive layer of 1 μm-thick hydrogenated amorphous silicon (a-Si:H). A 150 μm-thick spacer was used to vertically mount the two electrodes, forming a thin chamber within which bead/cell

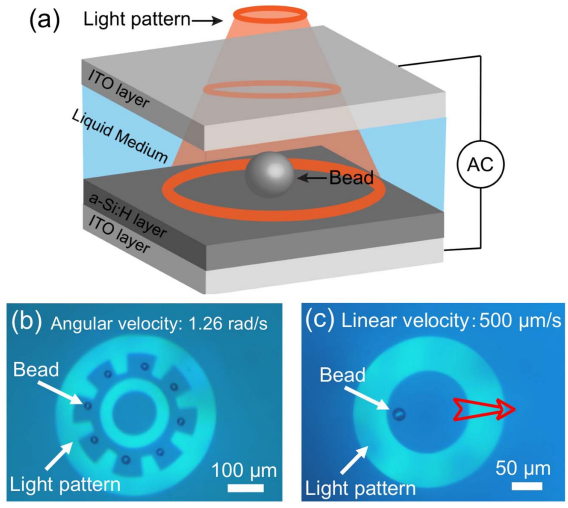

Fig. 1. (a) 3D schematic of an OET device. (b) Video frame showing the use of a "Roulette"-shaped light pattern to rotate 15 μm-diameter polystyrene beads. See Visualization 1. (c) Video frame showing the use of a "doughnut"-shaped light pattern to move a single 15 μm-diameter polystyrene bead at a linear velocity of 500 μm/s. The red arrow represents the moving direction. See Visualization 2.

manipulation was performed. OET devices are capable of performing micromanipulation because of the photoconductive properties of the a-Si:H layer. In the dark, the impedance of the a-Si:H layer is very high, and the applied potential drops mainly across this layer, leaving the liquid above mostly electric-field free. However, when the device is illuminated by light, the impedance of the photoconductive material drops significantly, and the voltage drops mainly across the liquid medium above the illuminated area. The resulting non-uniform electric field in the medium interacts with the samples in the liquid, producing either attractive force (positive DEP) or repulsive force (negative DEP) depending on the relative polarizability of the particle and the medium as described by the Clausius Mossotti (CM) factor [12]. Therefore, OET is very different from conventional optical tweezers that utilizes optical force based on the transfer of photon momentum [4].

In this work, we used spherical polystyrene beads (Polysciences, Inc., USA) of various diameters (3 μm, 4.5 μm, 7 μm, 10 μm, 15 μm, 20 μm, 25 μm, 30 μm, 45 μm, 60 μm, 75 μm) in deionized water containing Tween 20 (0.05% v/v) and MCF-7 breast cancer cells of various sizes (8 μm, 10 μm, 15 μm, 20 μm, 25 μm, 30 μm, 35 μm) in a sucrose buffer [8.5 wt% sucrose, 0.3 wt% glucose, 1.25% v/v phosphate-buffered saline (PBS)]. For the latter, large numbers of cells were scanned by eye to identify those with the desired diameters. Aliquots of bead or cell suspensions (20 μL) were pipetted into the chamber of the OET device, which was driven by an AC potential (20 V_{pp} 30 kHz sine wave for beads; 6 V_{pp} 20 kHz sine wave for cells). The optical setup is similar to that was previously reported [11], which consists of a digital micromirror device projector (Dell 1510X or Dell 1650) and a microscope (Olympus BX51 with motorized Prior Scan111 stage or Leica DM 2000 with motorized stage Märzhäuser Scan Plus 100 × 100). On applying the AC potential, the polystyrene beads and MCF-7 cells were repelled by the illuminated region due to negative DEP force [8]. This allows multiple beads or a single bead or cell to be manipulated using hollow light patterns, as shown in Figs. 1(b) and 1(c), respectively. For the parallel manipulation of multiple beads (Visualization 1), the motorized stage was kept stationary while a dynamic "Roulette" light pattern was used to rotate the beads. For the manipulation of a single bead or a single cell (Visualization 2), the "doughnut" light pattern was kept stationary, while the motorized stage was programmed to move linearly.

The maximum moving velocities of the differently sized polystyrene beads and MCF-7 cells were measured by gradually increasing the speed of the motorized stage until the trapped bead or cell was observed to fall out of the trap; the highest velocity for successful bead or cell transport was defined as the maximum velocity [13]. Figure 2(a) shows the relation between the maximum moving velocity and the square of the bead radius. The Reynolds number for the largest bead (75 μm diameter) moving at the maximum velocity in the OET device was calculated to be 6.5×10^{-2}, suggesting manipulation was in the laminar flow regime. In this regime, when an object moves through the liquid by DEP, the DEP force is equal to the viscous drag force, which is given by Stokes' law: [6,8,11,13]

$$F_{\mathrm{DEP}} = F_{\mathrm{drag}} = 6\pi\eta r\nu, \tag{1}$$

where η is the viscosity of the liquid, r is the radius of the object, and ν is its velocity. Since gravity forces beads to sit

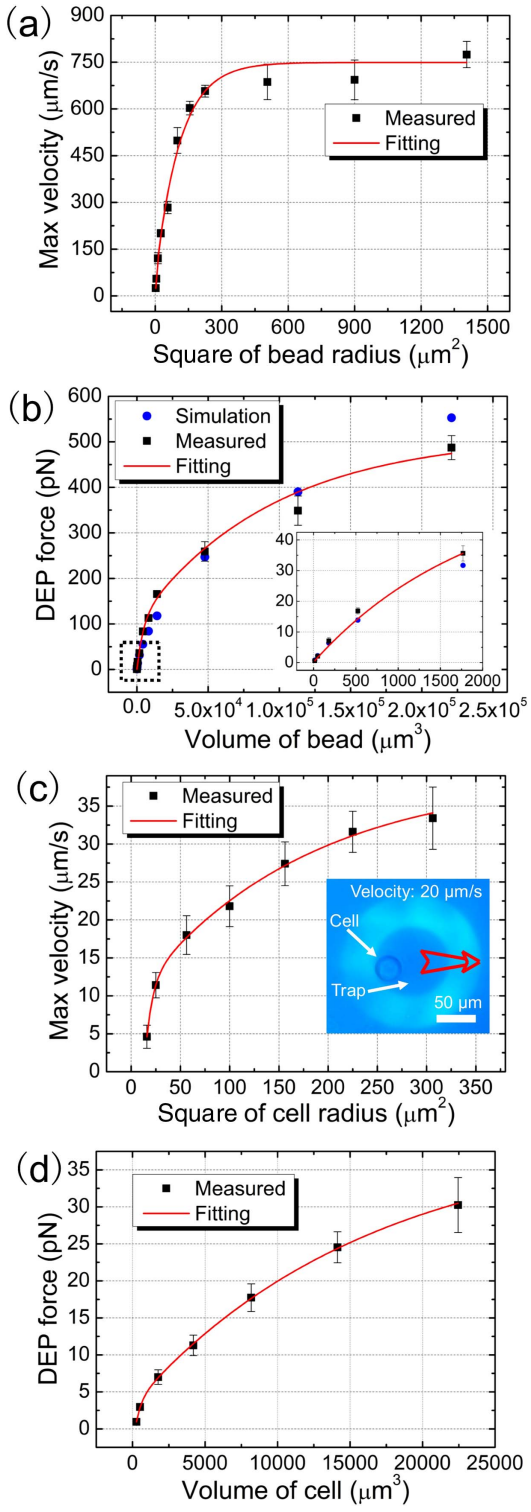

Fig. 2. (a) Maximum velocity versus square of polystyrene bead radius. (b) Measured and simulated DEP force versus polystyrene bead volume. The inset is a magnified view of the main-panel data in the dashed square. (c) Maximum velocity versus square of MCF-7 cell radius. The inset figure is a microscope image of a trapped cell moving at 20 μm/s. The red arrow represents the moving direction (see Visualization 2). (d) Measured DEP force versus MCF-7 cell volume. Error bars represent standard deviation for five replicates (for beads, each replicate was generated from a different bead; for cells, the replicates were repeated trials with the same cell).

in proximity to the a-Si:H surface (due to higher density of polystyrene beads compared with DI water), Faxen's correction based on the bead radius was used to adjust the calculation of viscous drag force and DEP force [8,11,14].

Based on classic dipole approximation theory for microspheres, the DEP force is given by [6,12,14]

$$F_{\mathrm{DEP}} = 2\pi r^3 \varepsilon_m \,\mathrm{Re}[K(\omega)]\nabla E^2, \tag{2}$$

where r is the radius of the object, ε_m is the permittivity of the medium, $\mathrm{Re}[K(\omega)]$ is the real component of the CM factor, and ∇E^2 is the gradient of the square of the external electric field. Figure 2(a) shows the relation between the maximum velocity and the square of polystyrene bead radius, and Fig. 2(b) shows the relation between the DEP force at maximum velocity and bead volume. In both relations, a similar trend is shown, where there is a large initial increase followed by a slow increase. In this case, there exist non-linear relationships between the bead size and the maximum velocity and DEP force. To have a better understanding of the trend, exponential fittings were also applied, as shown in Fig. 2 (red lines). These results suggest that the influence of the external electric field on beads, and the gradient of the electric field square (∇E^2), differ significantly with bead size. Similar phenomena were also observed for MCF-7 cells, as shown in Figs. 2(c) and 2(d), respectively. Therefore, similar non-linear phenomena were observed experimentally for two different bias conditions (20 V_{pp} 30 kHz for beads; 6 V_{pp} 20 kHz for cells) and two different types of objects (dielectric microparticles and biological cells), suggesting the underlying physical mechanism may be a universal one that applies for different samples and bias conditions.

To shed light on the observation of bead and cell behavior in OET traps, simulations were carried out in COMSOL Multiphysics. As shown in Fig. 3(a), the 3D model length (x axis), width (y axis), and height (z axis) are set to 200 μm, 200 μm, and 150 μm, respectively. A simple "trap" created by a light pattern is located at the bottom of the model ranging from 0–100 μm along x axis and from 0–200 μm along y axis. Other simulation parameters were set according to the OET device used in the experiments. Shown in Figs. 3(b)–3(d) are the distributions of simulated electric potential, electric field, and ∇E^2 (along x direction) of the cut plane in Fig. 3(a). In this model, it is assumed that a 15 μm-diameter bead is located at the edge of the trap (x coordinate of bead center: 107.5 μm; y coordinate of bead center: 100 μm). This setting is based on the observed experimental phenomenon that the bead reaches its maximum velocity at the edge of the light pattern before escaping the trap. As shown, there is a large potential change at the edge of the trap resulting in a region of strong electric field with sharp field variation at the bottom of the bead, caused by the difference in conductivity between the illuminated and dark a-Si:H surface [1]. Figure 3(e) shows simulated ∇E^2 as a function of the height of the cut line in the inset of Fig. 3(d), which starts from the bottom of the bead vertically to its top. As shown, the ∇E^2 drops significantly as the height of the cut line increases. Similar simulation results were produced for all other bead sizes.

Previous work reported the use of simulated ∇E^2 at the center of a bead to estimate the DEP force acting on the bead, [14] which is reasonable for small spherical microparticles with little electric field variation across the particles. However, this method is not applicable for the size-scaling experiments described here, as ∇E^2 varies significantly across the beads with large sizes. Other work reported the use of a surface integral of the Maxwell stress tensor (derived from surface charge and Lorentz force law) to calculate the DEP force [10,13], which can provide reasonable numerical results but at the cost of long simulation time. In this work, we have chosen a more intuitive

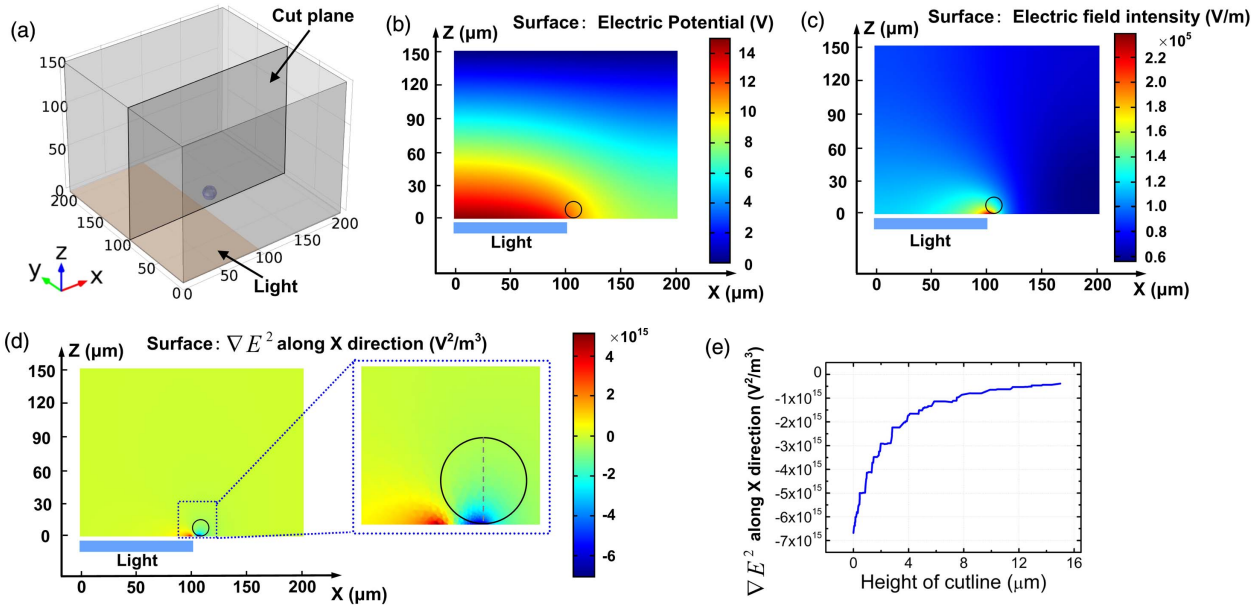

Fig. 3. (a) 3D simulation model and plots of (b) simulated electric potential, (c) simulated electric field, and (d) simulated ∇E^2 for an OET trap formed by illuminating a light pattern [shaded in brown in panel (a)] on the photoconductive layer of an OET device. The $z - x$ cut plane in (a) forms the basis for the plots in (b)–(d), in which the simulated electric potential, electric field, and ∇E^2 are plotted in heat maps (blue = low, red—high). In (b)–(d), the bead (15 μm diameter) is illustrated as an open black circle. The inset in (d) is a magnified view of the main-panel data in the dashed square. (e) Simulated ∇E^2 as a function of the height of the cut line. The cut line is shown in the inset of (d), starting from the bottom of the bead to its top.

approach where we consider how the gradient of the electrical field squared should vary over the volume of a trapped object, which has the benefit of allowing us to visualize how the forces vary across the bead. In this approach, we take the integral of the simulation of ∇E^2 over the bead volume ($\iiint \nabla E^2 \mathrm{d}v$), which accounts for the variation of ∇E^2 across the bead. Using this method, where ($F_{\mathrm{DEP}} = \frac{3}{2}\varepsilon_m \mathrm{Re}[K(\omega)] \iiint \nabla E^2 \mathrm{d}v$), the DEP force was calculated for different bead sizes. The results of this simulation are plotted in Fig. 2(b) (blue circles), which provide a qualitative match to the experimental observations.

Based on the simulations, the volume integral of the simulated ∇E^2 divided by bead volume was produced for all bead sizes: $\nabla E^2_{\mathrm{Simulation}} = \frac{\iiint \nabla E^2 \mathrm{d}v}{\frac{4}{3}\pi r^3}$. To compare the simulation results with the experimental results, ∇E^2 were also calculated based on the experimentally measured DEP force, and other experimental parameters [radius of the bead, permittivity of the medium, and the real part of the CM factor ($\nabla E^2_{\mathrm{Measured}} = \frac{F_{\mathrm{DEP}}}{2\pi r^3 \varepsilon_m \mathrm{Re}[K(\omega)]}$)]. Figure 4(a) compares the measured (black squares) and simulated (red circles) ∇E^2 for the polystyrene beads as a function of radius. As shown, the simulation data consistently match the experimental data and provide useful intuition about the effect of bead size on ∇E^2. The simulation shows that $\nabla E^2_{\mathrm{Simulation}}$ decreases as the bead size increases, causing a non-linear relationship between the bead volume and the DEP force. As the bead volume increases, the volume integral ∇E^2 does not increase jointly because of the non-uniform distribution of the ∇E^2. As shown in Figs. 3(c) and 3(d), there is a steep electric field gradient only in a small region near the bottom of the bead. This indicates that the DEP force experienced by the bead originates primarily from its bottom (close to the a-Si:H surface), while the top part of the bead makes little contribution to the overall DEP force. In contrast, of course, the viscous drag is homogeneous across all parts of the bead (with the exception of the region immediately adjacent to the solid surface), leading to the behavior observed in Figs. 2(a) and 2(b). This understanding should also apply to cells with different sizes as well as other dielectric samples (silica, PMMA, etc.). Most importantly, this result is insightful for the design of micro-actuators and micro-tools that OET can control. According to the analysis described above, micro-tools best suited for manipulation by OET can be large in the x and y dimensions, but should be short in the z dimension. In light of the clarified physics, one such tool, an OET-driven micro-rotor, was successfully developed as shown in Figs. 4(b) and 4(c). Note that the dimensions of this object (120 μm diameter; 25 μm height) make it challenging to manipulate by standard optical tweezers. OET can be used to rotate the micro-rotor at an angular velocity of 3.14 rad/s (or 0.5 rps, see Visualization 3), which may be useful in hydrodynamic or microfluidic applications [15,16]. We plan to optimize the design of the micro-rotor and explore its applications in the future.

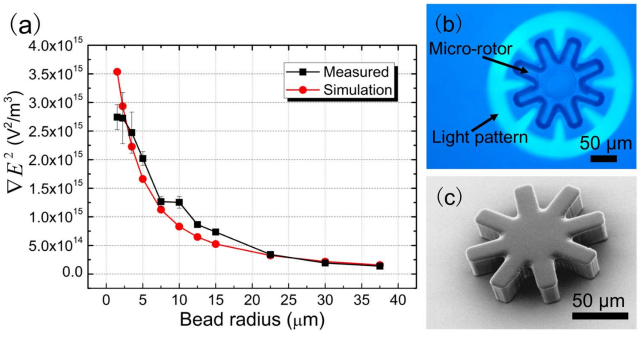

Fig. 4. (a) Measured (black squares) and simulated (red circles) ∇E^2 for polystyrene beads as a function of radius. (b) Microscope image of a micro-rotor in OET system. See Visualization 3 for a micro-rotor rotating at 3.14 rad/s and 1.26 rad/s. (c) Scanning electron microscope image of a micro-rotor.

In conclusion, we studied the size-scaling effect of polystyrene microbeads and MCF-7 cells manipulated by OET. It was found that for large particles, there exists a non-linear relationship between the bead/cell volume and the DEP force, caused by the non-uniform distribution of the electric field and the field gradient in the OET device. A method based on the integral of the simulated ∇E^2 over the bead volume was used to calculate the DEP force imposed on the differently sized beads, which matched well with the measured results. This work shows how OET is able to move large particles/micro-tools and provides useful information about how the forces on polystyrene microbeads and biological cells vary over different sizes. The physical mechanism we have observed allows insight into OET-based manipulation of other differently sized dielectric micro-objects and biological samples, and also for the design of micro-tools that OET can control.

Funding. Engineering and Physical Sciences Research Council (EP/L00044X/1, EP/L022257/1); Natural Sciences and Engineering Research Council of Canada (CREATE 482073-16, RGPIN 2014-06042, RTI 2019-00300).

REFERENCES

1. P. Y. Chiou, A. T. Ohta, and M. C. Wu, Nature **436**, 370 (2005).
2. A. Jamshidi, P. J. Pauzauskie, P. J. Schuck, A. T. Ohta, P. Y. Chiou, J. Chou, P. Yang, and M. C. Wu, Nat. Photonics **2**, 86 (2008).
3. H. Hwang and J. K. Park, Lab Chip **11**, 33 (2011).
4. M. Woerdemann, C. Alpmann, M. Esseling, and C. Denz, Laser Photon. Rev. **7**, 839 (2013).
5. A. Jamshidi, S. L. Neale, K. Yu, P. J. Pauzauskie, P. J. Schuck, J. K. Valley, H. Y. Hsu, A. T. Ohta, and M. C. Wu, Nano Lett. **9**, 2921 (2009).
6. S. M. Yang, T. M. Yu, H. P. Huang, M. Y. Ku, L. Hsu, and C. H. Liu, Opt. Lett. **35**, 1959 (2010).
7. I. Elvira, J. Muñoz-Martínez, Á. Barroso, C. Denz, J. Ramiro, A. García-Cabañes, F. Agulló-López, and M. Carrascosa, Opt. Lett. **43**, 30 (2018).
8. S. Zhang, N. Shakiba, Y. Chen, Y. Zhang, P. Tian, J. Singh, M. D. Chamberlain, M. Satkauskas, A. G. Flood, N. P. Kherani, S. Yu, P. W. Zandstra, and A. R. Wheeler, Small **14**, 1803342 (2018).
9. J. Matarrubia, A. García-Cabañes, J. L. Plaza, F. Agulló-López, and M. Carrascosa, J. Phys. D **47**, 265101 (2014).
10. J. Juvert, S. Zhang, I. Eddie, C. J. Mitchell, G. T. Reed, J. S. Wilkinson, A. Kelly, and S. L. Neale, Opt. Express **24**, 18163 (2016).
11. S. Zhang, J. Juvert, J. Cooper, and S. L. Neale, Sci. Rep. **6**, 32840 (2016).
12. R. Pethig, Biomicrofluidics **4**, 022811 (2010).
13. S. Zhang, A. Nikitina, Y. Chen, Y. Zhang, L. Liu, A. G. Flood, J. Juvert, M. D. Chamberlain, N. P. Kherani, S. L. Neale, and A. R. Wheeler, Opt. Express **26**, 5300 (2018).
14. S. L. Neale, M. Mazilu, J. I. B. Wilson, K. Dholakia, and T. F. Krauss, Opt. Express **15**, 12619 (2007).
15. D. Palima and J. Glückstad, Laser Photon. Rev. **7**, 478 (2013).
16. S. Mohanty, Lab Chip **12**, 3624 (2012).